===

Integration of geological and geophysical data for delineating groundwater potential zones at highly faulted area: a case study Cairo-Suez district, Egypt

Mohamed Elnahal[1]

[1]Geology Department, Faculty of Science, Zagazig University, Egypt
Corresponding author: m.elnahal23@science.zu.edu.eg

ABSTRACT : New Obour City was recently established on the Cairo-Suez District Road, which claimed to rely on groundwater resources. The geological structure has substantial control over the occurrence or distribution of underground water and water flow. In this study case, the integration among the drilling borehole data, structure, and direct current resistivity DCR soundings data figure out accurate geo-electrical sections of faults and the potential zones of underground water. This approach was applied, considering the complex tectonic history and the surface geological map. It is better to use the Schlumberger array, in this case, to obtain valuable information with a good signal-to-noise ratio and resolution about the subsurface hydrogeological conditions, which, using the genetic algorithm approach, solves the uncertainty of the CDR inversion problem and also provides a reference to data from available boreholes. The final output consists of the primary geological lithology, which, according to the deference in layer sequence, indicates structural faults according to the analysis of field structure data. The resistivity approach determines the occurrence of underground water and the aquifer geometry.

I. INTRODUCTION

In any society, water is a crucial requirement for social, environmental, and economic development (1) (e.g., Anomohanran et al., 2017). Recently, scarcity of surface water has increased, especially in arid countries (e.g., Egypt), due to existing reserves depletion, pollution, and increased demand. On the other hand, groundwater is the primary freshwater source for agricultural, new urban development, and domestic use in many areas of the world, especially areas with inadequate surface water resources. However, overuse of groundwater sources causes several kinds of environmental and engineering problems (e.g., saltwater intrusion and subsidence) if groundwater is being drawn faster than natural recharge (2) (e.g., Crestani et al., 2022). Furthermore, climate change can change temperature and groundwater levels and pose an additional risk to water supply and groundwater that is not yet understood. Accordingly, it needs attention to find adaptation solutions.

Groundwater exploration is a thought-provoking scientific work. The applied groundwater prospection methods should be well understood as a practical decision-making approach considering the surface geological conditions.

In general, groundwater occurrences vary from formation to formation. For example, the groundwater occurrences in sedimentary rocks are more promising than in crystalline, fractured, and weathered rocks. To explore the groundwater, many surface and subsurface techniques have been developed. The surface methods include remote sensing (3) (e.g., Abotalib et al., 2021), geological and structural (4) (e.g., Attwa et al., 2021), and geophysics (5) (e.g., Lawal et al., 2022). Geophysical and geo-electrical methods are widely used for groundwater exploration where the electrical properties of soils depend mainly on water content and salinity. Specifically, the direct current resistivity (DCR) method has been extensively applied for detecting the layer boundaries/structures and groundwater exploration/pollution (6) (e.g., Gupta et al., 2019). On the other hand, the

subsurface techniques for groundwater exploration include test drilling and borehole geophysical Logging. Compared with the aforementioned surface techniques, the subsurface techniques are costly and time-consuming. However, the subsurface methods are accurate because they help directly observe aquifers and measure their physical properties.

Many authors have discussed the geomorphology, structure, and hydrology in the study area; Barron (1907) discussed the geomorphology and the lithology of CSD by extracting geological map scale 1:25,000 and seven cross-sections along CSD, which recorded sediments ranging from Middle Eocene to Holocene, also assigned a post-Miocene age affected with (E-W and Clysmic NW-SE) faults. On the other hand, basalt and the silicification processes in the CSD in the pre-Miocene time were discussed. El-Fayoumy (1968) discussed the hydrology in the east of the Nile Delta (CSD), which subdivided into several hydro-stratigraphic units, the Quaternary aeolian sand aquifer, the Miocene sandy aquifer, the Oligocene basalt aquifer, the Oligocene fluviatile aquifer, the Eocene calcareous aquifer and the cretaceous of Nubian facies aquifer. El-Shazly (1975), discussed the structure of CSD by using a geophysical survey (Aeromagnetic survey), which recorded that CSD is represented by a complete wave of anticline and syncline folds, which are controlled by the hydrogeological system. El Shazly (1981) recorded faults of trends NE-SE, ENE-WSW, NE-SW, and E-W. which notable fold in Oligocene (Gebel Al Ahmer formation) at Gebel Hamza. Sallouma (1983) described the hydrogeology and hydrochemistry of water resources east of the Nile Delta, which, signed to the Quaternary deposits, represent the principal groundwater Aquifer; the general direction of groundwater flow is SW to NE. Diab (1984); and Khalil (1988) recorded two groups of aquifers in the eastern part of the Nile Delta (CSD). The main aquifer is a semi-confined Quaternary aquifer bounded by the Damietta branch and Ismailia Canal. The second group is an unconfined aquifer, recorded in Quaternary, which indicates the salty water mixed with the fresh water in CSD. Boulos (1986) studied the electrical resistivity sounding, which noticed the presence of two conductive geoelectric layers, probably Water-bearing the Midway in the CSD road. Duo to the outcropping of basalts in the study area using a Magnetic survey. Khalil and Atta (1986) studied geology and hydrology between Ismailia Canal and Ismailia desert road. Signed groundwater salinity distribution affected by freshwater seepage from the Suez Canal and its attached lakes. Khalil (1988), discussed that the groundwater of the eastern part of the Nile Delta occurred two groups of aquifers. The main aquifer is Quaternary aquifer. Abu El Ezz (1992) described the morphological features, which pointed to the Miocene clay deposits from Gebel El-Hamza to Gebel Um-Qamar and represented very important in the cement industry. EL-Mahmodi (1995), based on a geoelectric resistivity study, the sandy Pleistocene aquifer in the eastern Nile Delta comes from the freshwater by Ismailia Canal and Domietta Nile branch. Also, the Aquifer feeding by trending NE irrigation canals. Hussein (2001) reported that the subsurface Eocene water-bearing information is limited in the eastern part of CSD (Gebel Hamza). Attwa and Henish (2018) used the integration between structure and geophysical data (DCR, ERT), which, complex structure faults and folds represent the CSD. Thus, the CSD represents a new development axis for Urban and Industrial expansions. Attwa, Henish, and Zamzam (2020) studied hydrology in the northern part of CSD by integrating structure and geophysical data. The study area is represented by three main aquifers (Miocene, Oligocene, and Eocene), which by using SGR, there are 52 points at 0 depth along normal faults affecting the study area. Henaish, A., Kharbish, S., (2020). Linkage style of rift-associated fault arrays: insights from central Cairo-Suez district, Egypt. Attwa, Henish, and Zamzam (2023) integrated structural geophysical and remote sensing data to characterize extensional linked fault systems and related land deformation hazards in Cairo-Suez District, Egypt.

New communities and land reclamation projects have been recently established (e.g., New Cairo and Obour cities) along Cairo-Suez District (CSD), Egypt. CSD is a highly deformed region (7) (e.g., Attwa and Henaish et al., 2018) and, consequently, groundwater potentialities assessment is vital for land reclamation activities (Urban and agriculture land) at such desert land. (8) (e.g., Attwa et al., 2020) studied the structural controls on aquifers distribution at CSD. Geologically, CSD is covered by many rock units related to the Oligocene, Miocene, and Eocene periods. In addition, many fault and fold structures can be well recognized. Accordingly, understanding such regions' geological and structural conditions is a substantial task for exploring aquifers.

In the present work, an integrated approach of geological and geo-electrical data is introduced to assess the geological and groundwater conditions at a new urban city as a case study, along CSD (Fig.1). The study includes geological and geophysical, using the DCR method, surveys. The suggested approach aims to link the surface geological and structural data with the deduced structures from geophysical inversion results to assess the groundwater potentialities in such an arid region. Finally, the significance of our findings for environmental applications is discussed.
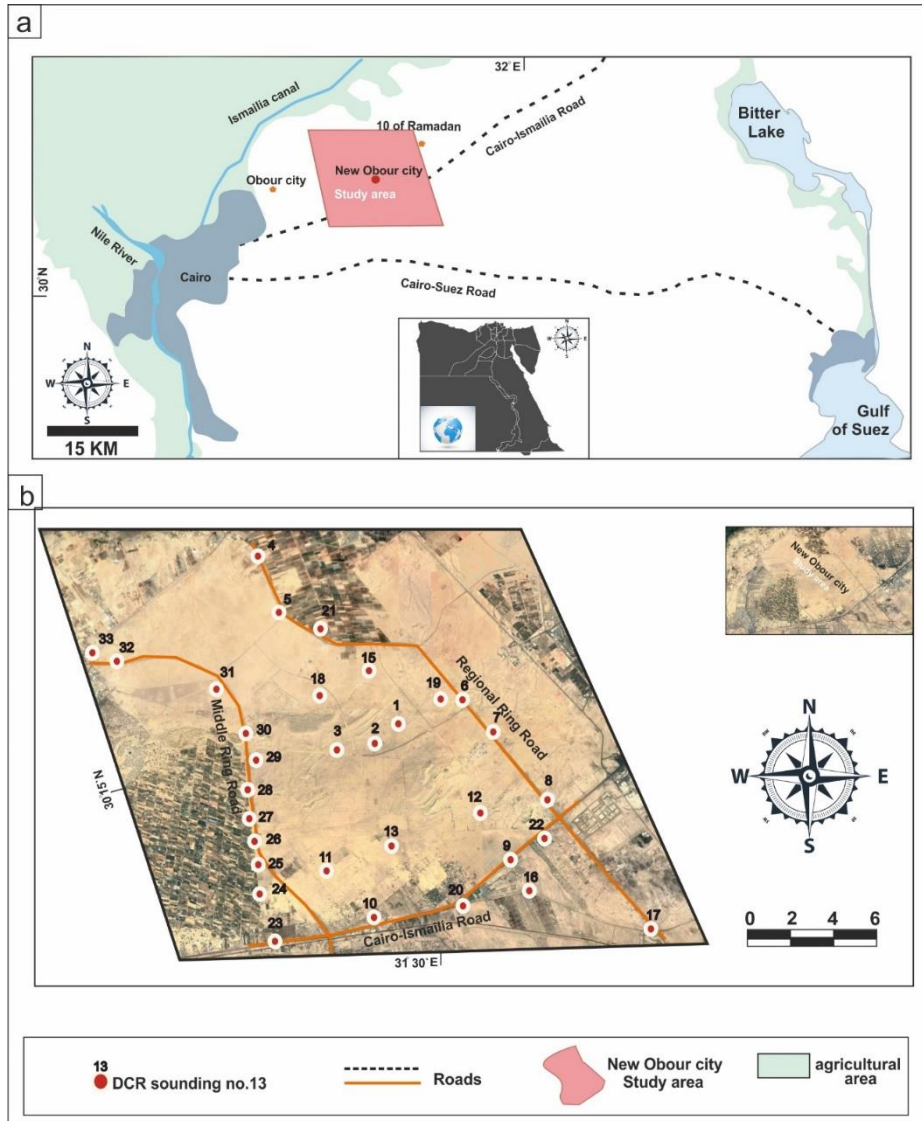
Fig. 1. (a) Location map of the study area and (b) Google Earth satellite image (2022) with DCR soundings location at the study area.
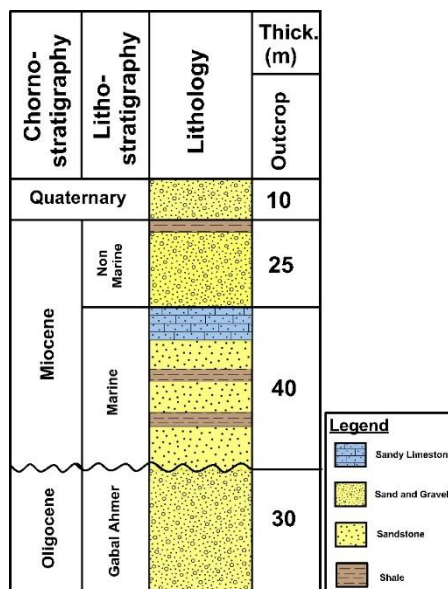
II. STUDY AREA AND LOCAL GEOLOGY

The study area represents a new urban area named New Obour City, which is located in the northwestern part of CSD between Obour and 10th of Ramadan cities (Fig. 2). Geologically, the study area represents a division of the Northern Eastern Desert and comprises a highly deformed area with a complex tectonic history.
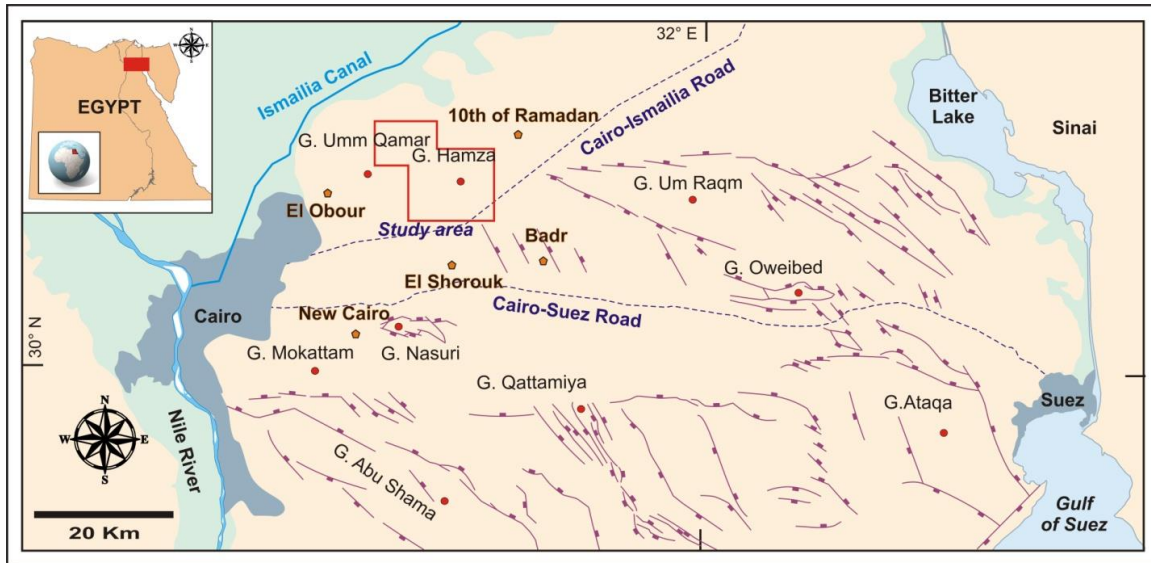
Fig. 2. The major structures of the simplified tectonic map of Cairo-Suez District (CSD) (compiled from (Moustafa et al. 1985; Moustafa and Abd-Allah, 1991; Attwa and Henaish, 2018). (9,10,11)

Stratigraphically, the outcrops of the study area are represented by four central rock units: Oligocene, marine Miocene, non-marine sediments, and Quaternary sediments. The oldest exposed rock unit is represented by the Oligocene Gebel Ahmar Formation, which consists of vividly colored, coarse-grain, mostly friable sandstone and gravel bands of limited extension. It is overlain by the marine Miocene rocks, which comprise calcareous sandstone, shale, sandy limestone, and marl. The non-marine Miocene overlies the marine Miocene sediments and comprises gravels and sands with clay intercalations. The Quaternary sand and gravel overlaying the exposed rock units in several places also show the maximum aerial distribution in the southern part of the study area.


Fig. 3. Composite stratigraphic section showing the local geology of the study area r (Henish and Attwa, 2020). (12)

Structurally, the investigated area represents a part of the northern CSD at which sedimentary rock units' distribution is structurally controlled. Many steps have been followed to figure out the structural setting of the area. Firstly, the regional setting has been investigated via satellite images to delineate the regional structures and characterize lithological variations. Secondly, several field trips have been encountered to record and measure locations and geometries of the investigated field geological structures. Also, attitudes of bedding

planes have been recorded. During this stage, high-resolution Google Earth images have been used to plot filed data in their exact location (Fig.4). Finally, field data have been plotted and drawn to introduce a structural map of the area.

Tectonically, the present-day structural setting at CSD, including the area under investigation, is controlled by several tectonic events as a result of the relative movements between the African, Eurasian, and Arabian plates (e.g., Attwa and Henaish, 2018; Henaish et al., 2022). (11,13) Moreover, the CSD registered three main tectonic events, including the Jurassic rifting, Late Cretaceous transgression, and Oligo-Miocene rifting of the Gulf of Suez (e.g., Henaish 2018a; Henaish and Kharbish et al., 2020). (14.15) These tectonic events are responsible for the structural shaping of CSD, including E-W extended fault belts of en echelon normal faults (e.g., Moustafa et al., 1998). (16) Also, the general trends of the registered faults area are mainly oriented toward the NW-SE, E-W, and NNW-ESE (e.g., Henaish, 2018 b; Attwa et al., 2020). (17.18)
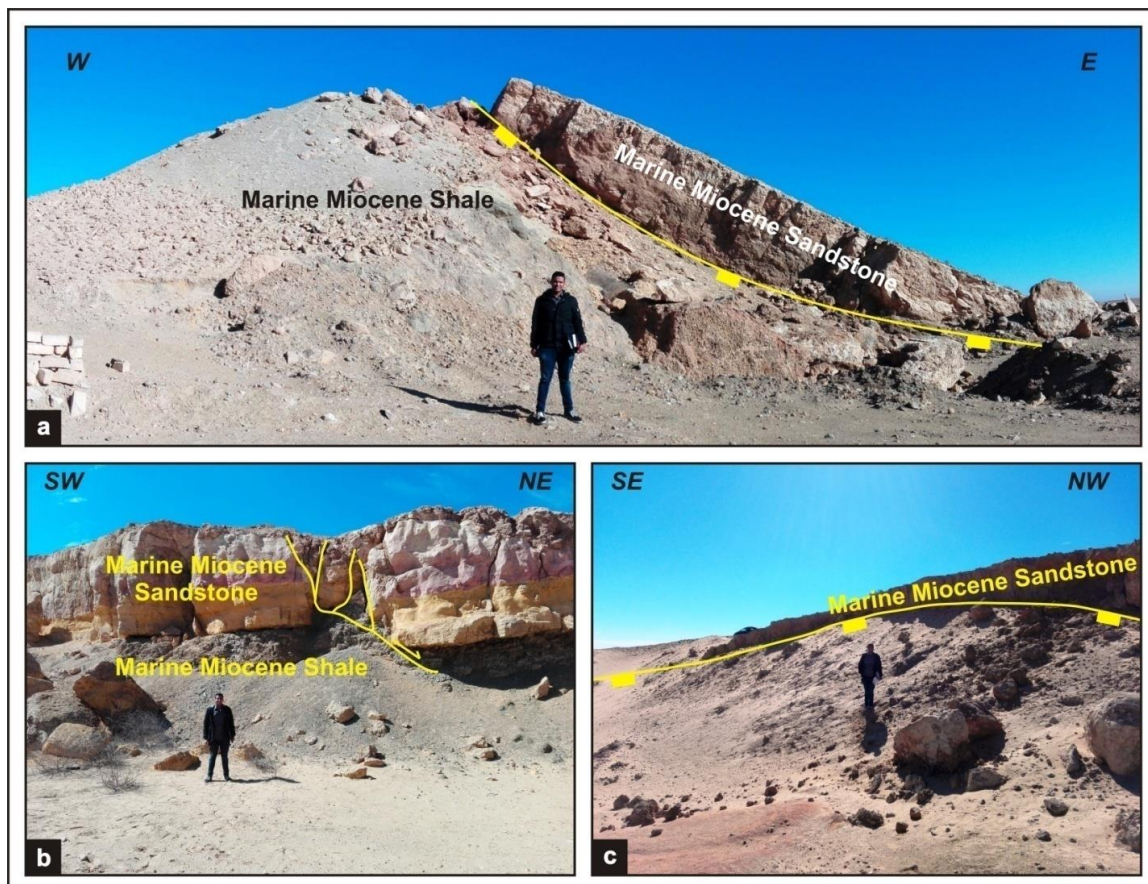
Fig. 4. Field photos showing examples of field-investigated faults that cut the Miocene rocks.

Hydrogeologically, the study area belongs to the Heliopolis, ELGafra, and Belbays basins, which feed with water from the Damietta branch (Fig.5). The groundwater in the northern part of CSD is represented by the Pleistocene aquifer, which the center and west of CSD represented by the Miocene, Oligocene.
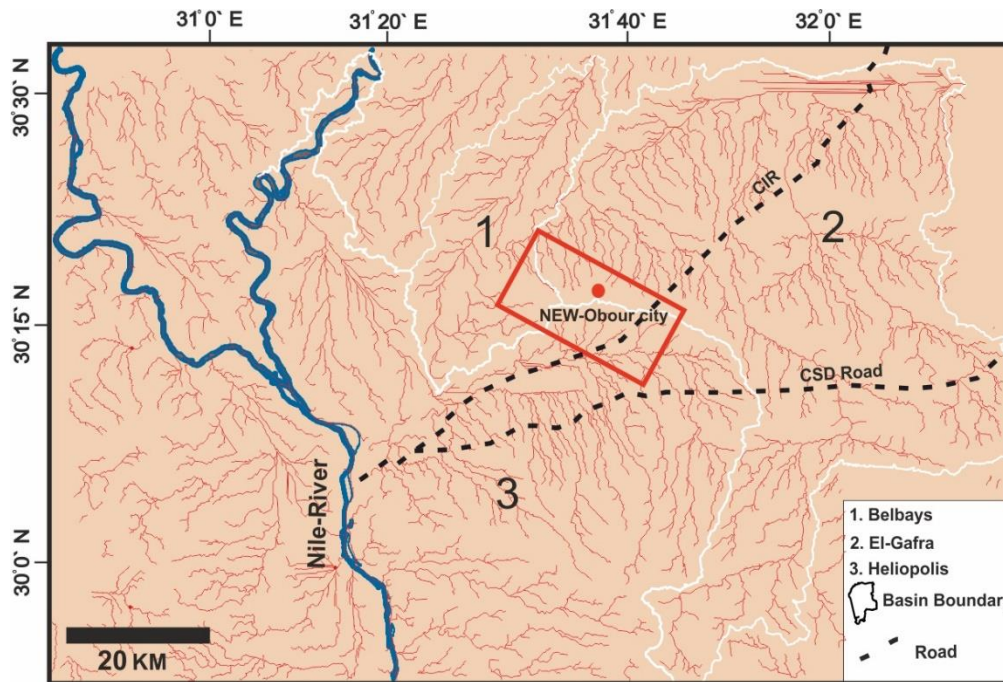
Fig. 5. Hydrographic Basins of The New-Obour City overlaid on STREM DEM

a) Quaternary aquifer (Pleistocene):

The Quaternary deposits are storage and expressed as the most important aquifer of CSD, which is very limited in new Obour city and recharged mainly by some of the eastward outflows of the Nile delta aquifer, in addition to the recharge through the drainage lines within the Heliopolis basin (Fig 4). (e.g., Attwa and Henaish et al., 2020). (18) The thickness of the Pleistocene increased in the north of the new Obour city. (Fig.3). the Pleistocene aquifer consists of sand, gravel, and fragments.

b) Miocene aquifer:

The Miocene aquifer mainly extends along the CSD area in both Heliopolis and El-Gafra basins (Fig 4); in El Obour city, the Miocene sediments are found overlying the Oligocene basalt and controlled by complete structures such as faults and folds (e.g., El Haddad et al., 2002). (19) The permeability value of the Miocene aquifer is relatively lower than the Pleistocene aquifer according to the lithostratigraphy. (Fig 3).

c) Oligocene aquifer:

The Oligocene and Miocene aquifers were delineated at CSD's central and western parts. (e.g., Attwa, Henaish and Zamzam et al., 2020) (18), which is controlled structurally by faults. (e.g., Abuo Heleieka and Atwia et al., 2015). (20) The Oligocene aquifer is mainly composed of sand with interbedded few clays intercalation and basaltic sheet. The Oligocene aquifer is recharged chiefly from the southern watershed areas (e.g., Gebel El-Ahmar, Gebel Yahmoum El-Asmar). On the other hand, the Oligocene sediments are exposed in the Heliopolis basin according to the tectonic framework.

III. GEOPHYSICAL DATA ACQUISITION, PROCESSING, AND INVERSION

DCR technique is a fast and cost-effective method used to construct credible hydrogeological information according to structure and geological models (Gouasmia et al., 2018; Attwa et al., 2021). (8,21) The DCR soundings were acquired using a GD-20 resistivity meter (Geomative instruments). The ID direct current resistivity DCR technique theoretically requires electrical current injection into the subsurface layers by a pair of current electrodes (AB). Then, the resulting variations in electrical potential are measured in other pairs of electrodes (MN). Electric currents were represented by stainless-steel electrodes bounded with salt water and bentonite around the poor electrode contact, according to the ground surface and aridity. The ground contact resistance was less than 10 kΩ. The measured (i.e., apparent) resistivity data were stacked 8 times, and final data were recorded when the data quality factor values were minimized (i.e., stacked error ~< 2%). Furthermore, standard deviation measurements of less than 4% were used for the interpretation process. Thirty-three DCR soundings were acquired using a conventional Schlumberger array with a maximum AB spacing of 2000 m. (e.g., Attwa and Ebong et al. 2021), (8,22) indicate that using the Schlumberger array in desert lands to obtain

valuable information with good signal-to-noise ratio and resolution about the subsurface hydrogeological conditions is better. The average spacing between every two successive resistivity-sounding stations along each line differs according to the area possibility. Figure (1b) shows the distribution of the measured DCR soundings at the New Obour city. The electrical electrode contact with the ground or instrument sometimes induces errors or noises. (e.g., Maury and Balaji et al. 2013). (23) The apparent resistivity data of DCR soundings were inverted by applying a sequential use of conventional (IPIWinsoftware) (e.g., Bobachev et al. 2008) (24) and non-conventional inversion schemes (genetic algorism, GA). (e.g., Baskar et al. 2007). (25) Generally, the non-conventional inversion approach increases the chance of getting accurate values to obtain the best model. (e.g., akca and Basokur et al. 2010). (26) The search space in GA was adapted considering the results of the conventional interpretation method and borehole information. (Fig.7) shows an example of the interpretation of DCR sounding No.22 using a conventional inversion scheme. Depending on such conventional inversion results using a 1D linear filtering and damped least-squares algorithm (Levenberg-Marquardt), the DCR soundings were inverted using a non-conventional inversion scheme applying GA. (Fig.6) represents the interpretation of DC sounding No. 22 using GA (for location c.f. Fig.1b). It can be observed that the generation number and population size were both 60. In the same way, the other DCR soundings were inverted using GA using the same generations and population number.
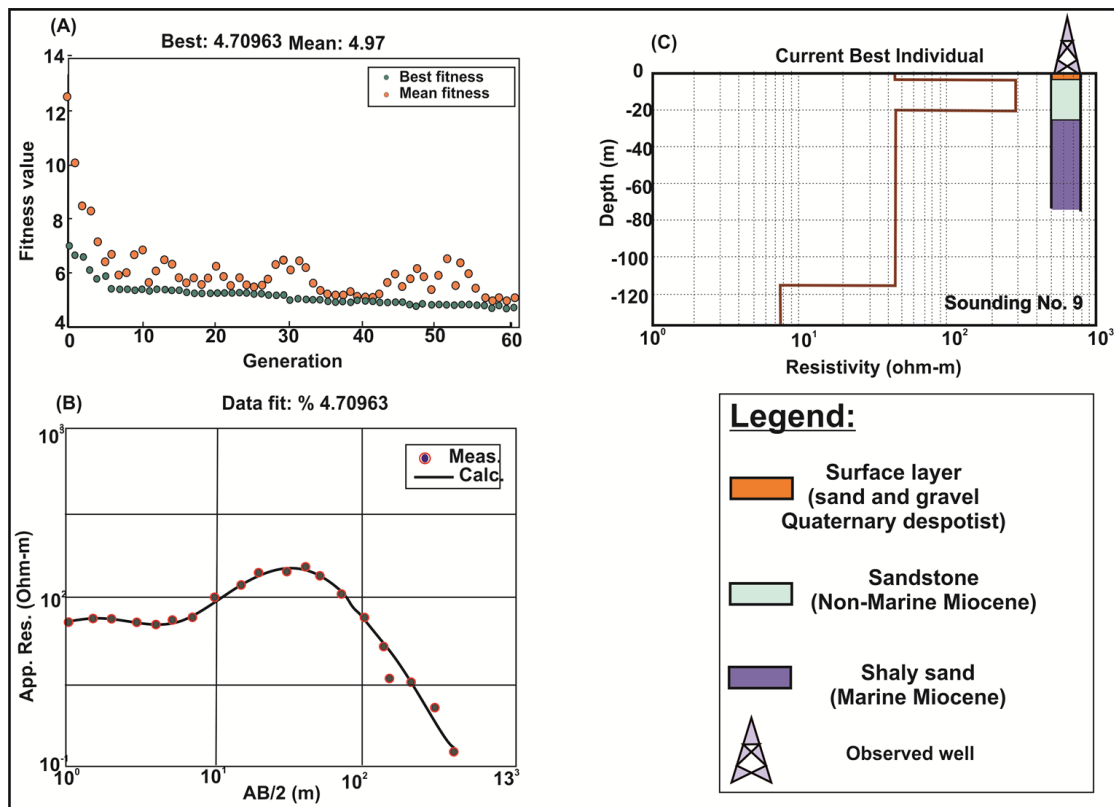

Fig. 6. Inversion results in DCR sounding point No. 22 applying GA (for location, c.f. Fig. 1b) with borehole data calibration.
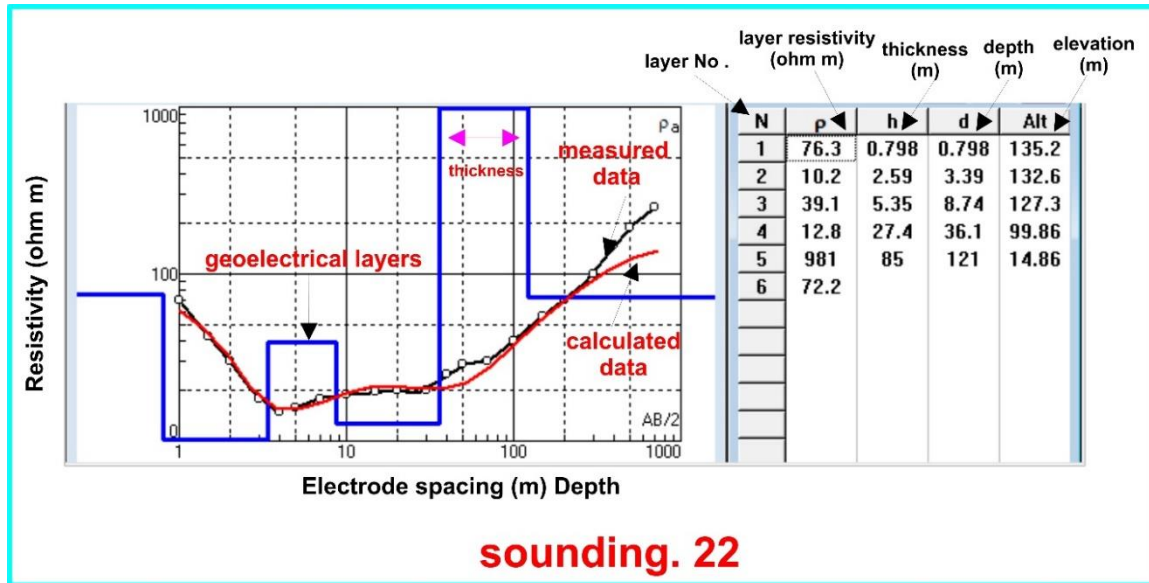
Fig. 7. Inversion process of DCR sounding.22 using a conventional scheme depending on a 1D linear filtering and damped least-squares algorithm (Levenberg-Marquardt).

IV. RESULTS AND DISCUSSION

Structurally, the study area represents a central doubly-plunging ENE-WSW oriented anticlinal fold with an Oligocene fold core and Miocene flanks. The recorded dip data of both flanks revealed gentle dip values of bedding planes (5°-15°) except near the fault surface where dip values exceed 25°. Faults are well characterized through field work where the types of the mapped faults are mainly normal faults. The measured dip angles of faults revealed moderate to steep dip angles that range from 65° to 80°. Most of the investigated faults are found dissecting the Miocene rock units. The analysis of the significant traced fault segments revealed three main trends: NE-SW, NW-SE, and ENE-WSW. Also, lengths of the mapped faults range from 3 to 10 Km on the map view. (Fig.8)
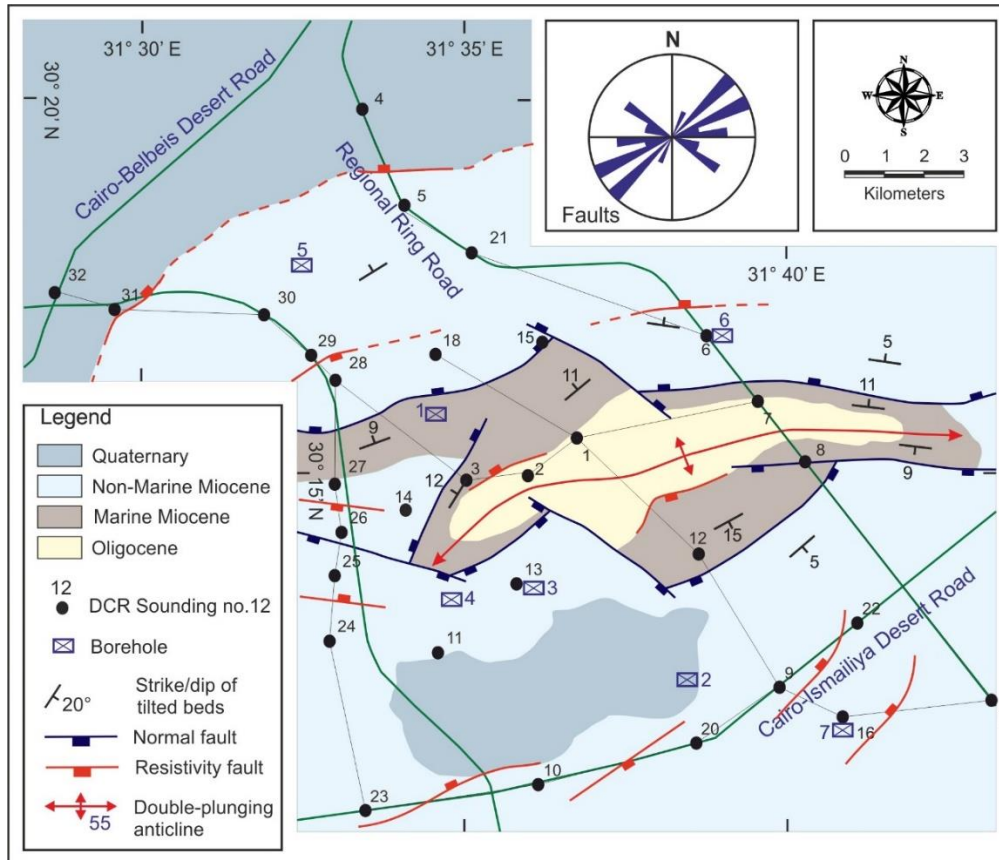
Fig. 8. The geological map and DCR sounding locations in the study area.

Based on the inversion result of DCR soundings, five resistivity sections (Fig.8) were designed to delineate the regional geology, structure, and hydrogeological setting considering the fault related to the Anticline fold structure in the study area, which the borehole information helped to overcome the DCR soundings opacity and to construct a connection among the geological information and interpreted resistivity data. According to our study, the resistivity sections A-A' and B-B' were built parallel to the fold axis in directions W-E, SW-NE. On the other hand, the resistivity sections C-C', D-D', and E-E' are perpendicular to the fold axis NW-SE directions (fig.8,9). Moreover, the output geological, structure geometrical parameters and available hydrogeological data are integrated to be considered in constructing the resistivity sections. The subsurface geological and structure mapping depends on the geo-electrical layers with defined lithology, thickness, and depth. According to the structural point of view, the change in resistivity values and thickness of the deduced geo-electrical layers can be attributed to the deformation of rocks. (e.g., Attwa and Henaish et al. 2020). (18)

Five main geo-electrical resistivity sections represent the study area. The first geo-electrical layer (yellow color) comprised a surface cover with an average thickness of (30) m represented by Quaternary. Geoelectrical surface layer resistivity ranges from low to high resistivity values (2 -1000 ohm-m), thus indicating the cover surface contains gravel, pebbly sand, rock fragments, and interbedded shale. The second geo-electrical layer is represented by medium resistivity (10-11 ohm-m) and consists of shale followed by non-marine Miocene with an average thickness of 30 m and is a recent lithography layer in (sounding no. 16-9). The third layer is represented by non-marine Miocene argillaceous sandstone with gravel increasing in thickness from NE to SW with a range of 30m in (Sounding no. 18) and 50 to 170 m from (Sounding no. 9) to (Sounding no. 17). The resistivity ranges from high to medium (45 to 250 ohm-m). The fourth geoelectrical layer is represented by light green, consisting of marine Miocene sandstone with a thickness of 50 m (Sounding no. 18), which is located in limps of the fold, and the resistivity ranges from high to medium (130 to 300 ohm-m). The fifth geoelectrical layer (medium green color) resistivity ranges from medium to high resistivity (50-120 ohm-m), consisting of marine Miocene argillaceous sandstone in (soundings no. 18-12) with average thickness ranges of 50m in (soundings no.12). The sixth layer is green (sounding no. 12) and consists of marine Miocene shale represented by low resistivity (2 to 15 ohm-m). The seven-layer underlies the Miocene layers and represents by

Oligocene, which consists of sand (sounding no. 1) and is located in the fold core. The Oligocene sand layer thickness average 120m in (sounding no. 1), and the resistivity values (< 400 ohm-m). The eighth layer underlies the Oligocene layer, consisting of Eocene limestone with shale interbeds with a resistivity range (120-300 ohm-m).

Structurally, the area represented by six normal surface faults and thirteen electrical faults, the cross-sections C-C', D-D,' and E-E' is perpendicular to the fold axis NW-SE directions, which normal faults affect the sequence of the layers. The surface fault is involved between VES 17 and VES 8 with an upthrow to the sand/ gravel Oligocene, which causes the difference in lithology in VES 17 sequence from recent Quaternary, non-marine Miocene argillaceous sandstone with gravel then Miocene sand according to a normal fault, on another side the VES 8 and VES 7 located in fold core represented by upthrow which contained the Oligocene sandstone as an old layer then the appearance of Eocene limestone with shale interbeds. On the other hand, the fault between VES 7 and VES 6 is deduced by the variation in electrical resistivity. The borehole 6 data with a downthrow toward VES 6 caused the increase in non-marine Miocene argillaceous sandstone with gravel thickness from 100m in VES 17 to 150m in VES 6 and disappear of the Oligocene layer in VES 6, indicating of horst fault in VES 8-VES7. The Horst Fault controlled the Oligocene and Eocene aquifers whose depth to water in borehole 6 reached 78m, and the downthrow of faults controlled the Miocene aquifers. Moreover, the fault between VES 16 and VES 17, deduced by the variation in electrical resistivity in correlation, resulted in the dipping fault toward VES 16. The Quaternary layer appeared on top of VES 17. In addition to the thickness variation between VES 16 and VES 9 in the non-marine layers, deduced resistivity fault with a dip angle of 10° toward VES 9. According to the borehole and surface, there is a surface fault between VES 9, representing non-marine Miocene, and VES 12, which is located in a fold limp and represents marine Miocene toward VES 9. On the other hand, the lithology between VES 12 is very different in resistivity in VES 1, and according to the difference in geology from limp to core fold that's interoperated resistivity fault toward the VES 12, which VES 1 represented by Oligocene overlayed Eocene layers and underlines marine Miocene layers with upthrow. The VES 18 is very near the fold limp. Thus, it is affected by a normal surface fault between it and VES 1 towards NE in VES 18. The resistivity fault between VES 24 and VES 25, which fault direction toward VES 25 with a downthrow; moreover, between VES 25 and VES 26 contains graben. On the other hand, between VES 26 and VES 27, with a downthrow toward VES 27; thus, it contains graben. The surface between VES 27 and VES 28 interprets the difference in layers thickness in these soundings. It contains horst, and VES 27 and VES 28 represent the Graben fault, which is the difference in thickness and slope of sequence layers deduced by a normal fault. The fault between VES 30 and VES 31, according to the downthrow toward VES 31 and the appearance of a Quaternary layer in VES 31. To complete the resistivity area studying, the cross-sections A-A' and B-B' were built parallel to the fold axis in directions W-E, SW-NE. The cross-section A-A' is parallel to the anticline fold and affected by three normal faults between VES 22 and VES 9, resulted in the variation in layers thickness according to the downthrow toward VES 9. In addition, between VES 20 and VES 10, which disappears from the shale layer, indicates the downthrow toward VES 20 and the upthrow of marine Miocene sandstone in VES 10 and between VES 10 and VES 23 which, the cross-section B-B' represented by three faults in the anticline fold core. The movements are languid in Oligocene, while the faults are more active in Miocene. The fault indicates that the Oligocene was affected by downthrow, and the Miocene layers began to appear. The anticline folds core and these normal faults controlled the underground water appearance. the variation of the resistivity values between VES 2 and VES 3 with a downthrow toward VES 3, which is represented by the Marine Miocene layer recently than the Oligocene layer in VES 2. On the other hand, the surface fault between VES 3 and VES 27, which the downthrow toward VES 27 and the appearance of a non-marine layer recently of marine layer in VES 3.

Hydrogeologically, according to the wells data, the depth to water increases from SW to NE shown in (Fig.10), from the boreholes studies the water table ranges +20 to -20 from sea level and the integration with the resistivity values and structure sitting resulted that the study area represented by three aquifers Miocene, Oligocene and Eocene. The Miocene aquifers in the limps of the anticline fold and around fold core. On the other hand, the Oligocene – Eocene aquifers located in the core of the anticline fold. The cross-section A-A' in the south of the study area represented by Miocene aquifers controlled by three faults, which resulted to the variation of water table from VES 22 reach to 120 m to VES 23 reach to 85 m depth. The cross-section B-B' located in the anticline fold core which represented by Oligocene – Eocene aquifer; the resistivity fault between VES 2 and VES 3 resulted in the Miocene aquifer. The depth to water in fold core ranges from 185m VES 7 to 125 m in VES 2 and in the limp of fold the water depth range for Miocene aquifer ranges from 125m in VES 3 to 180m in VES 29. The cross-section C-C's water table ranges from 85m in VES 23 then the fault decrease the water table to 50m in VES 25 and VES 26 which the Graben structure controlled the water table as EX. On the other hand, the water table reach 80m in VES 27 that controlled by horst fault. In VES 28 Graben fault resulted the increase in water table to 110m. In VES 29 and VES 30, the horst fault controlled the increasing of water table to reach 155m, moreover decrease in VES 31 and VES 32 to 135m, this cross section represented the

Miocene aquifer. The cross sections D-D' and E-E' passing through the anticline fold from limp to core, thus the variation in geological and aquifers controlled by structure setting being so clear. The horst faults in the sections controlled the Oligocene- Eocene aquifers with water table 140 m in VES 1, VES 7 and VES 8. The water table of Miocene aquifers in the south ranges from 180m in VES 17 to 85m in VES 23, in the north of study area the water table ranges from 65m in VES 4 to 135 in VES 32, Which in the central 150m ranges in VES 18 to 100m in VES 12. The water table of Oligocene- Eocene represented in anticline fold core with water table ranges from 185m in VES 7 and VES 8 to 160m in VES 1and VES 2. (Fig .10)
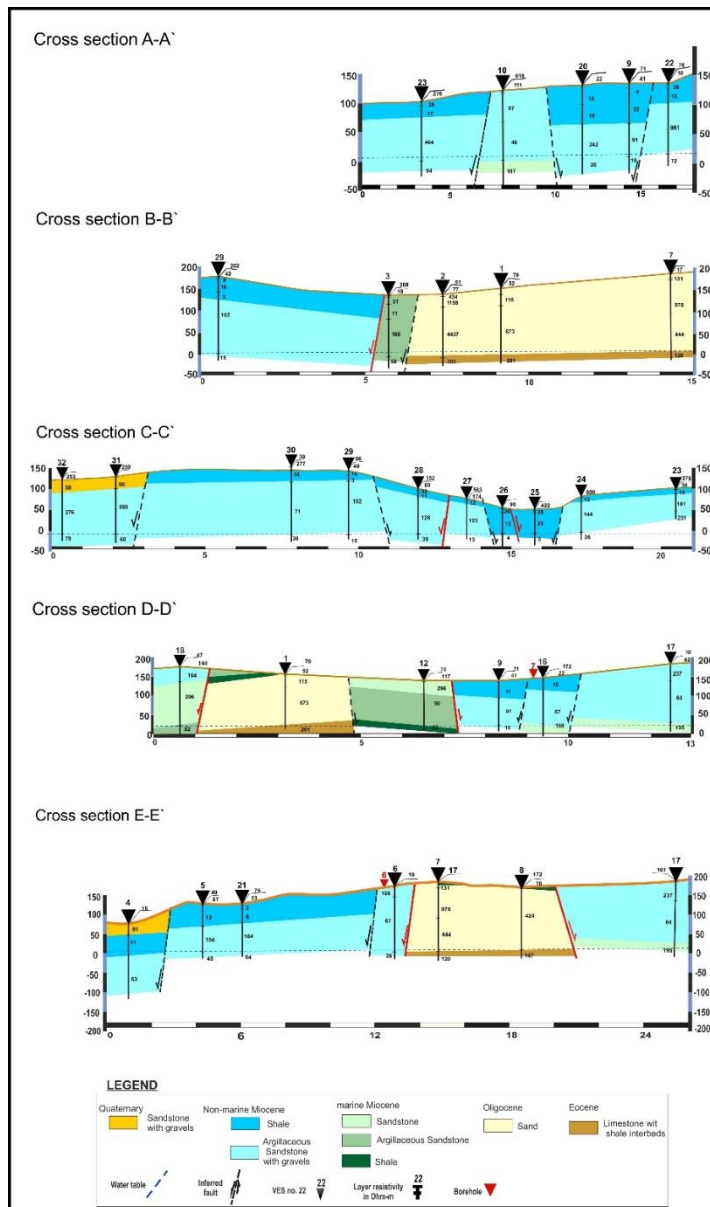
Fig. 9. The stitched resistivity sections resulted from DCR soundings inversion calibrated with outcrop and borehole data.
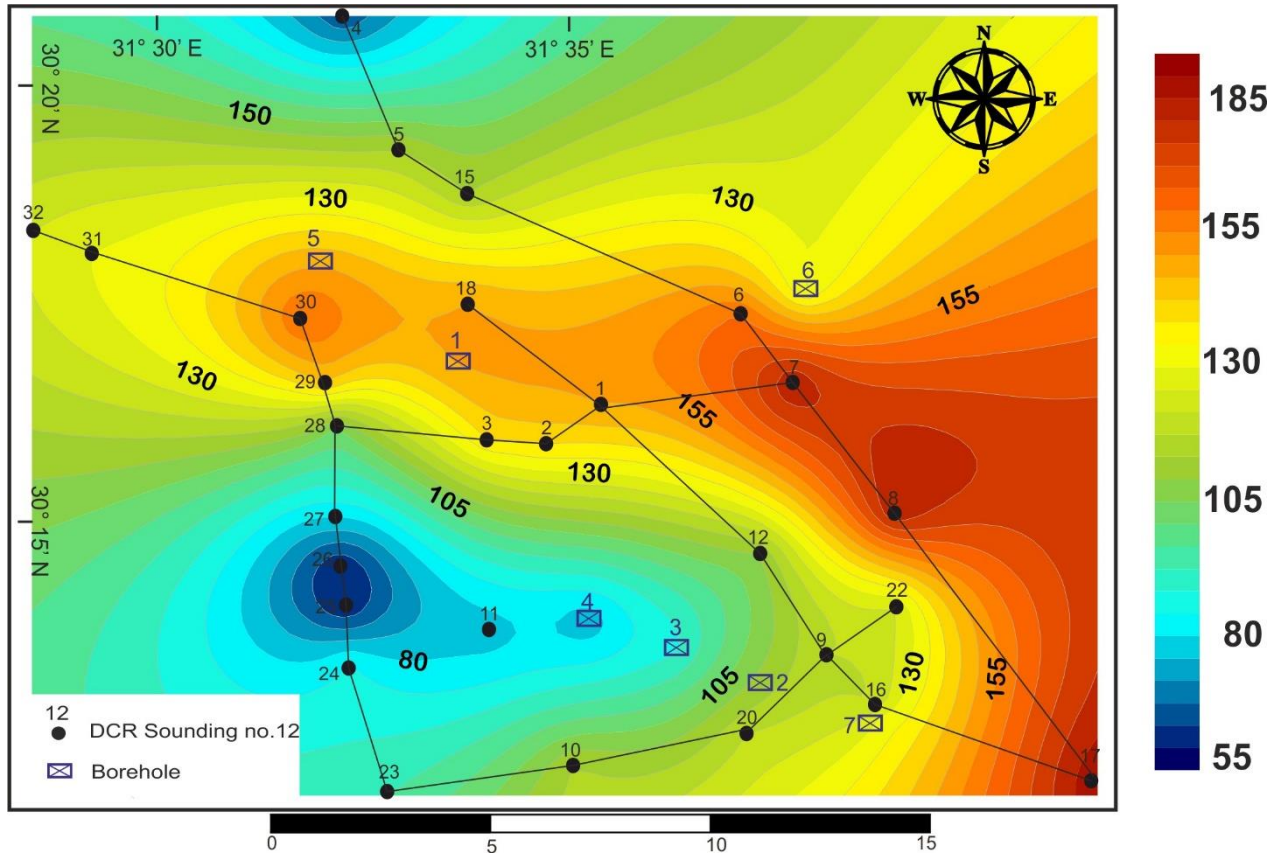
Fig. 10. contour map for depth to water according to the boreholes and DCR soundings.

CONCLUSION

The new Obour city relies on groundwater resources. The geological structure has substantial control over the occurrence or distribution of underground water and water flow. The result of the Schlumberger array obtains valuable information with a good signal-to-noise ratio and resolution about the subsurface hydrogeological conditions, which, the genetic algorithm approach, solves the uncertainty of the CDR inversion problem and also provides a reference to data from available boreholes. The resistivity approach determined the occurrence of underground water and the aquifer geometry. According to the study of structure in the New Obour City, a prominent doubly-plunging ENE-WSW oriented anticlinal fold has an Oligocene fold core and Miocene flanks. The recorded dip data of both flanks revealed gentle dip values of bedding planes except near the fault surface where dip values exceed to reach 25°. Faults are well characterized through field work where the types of the mapped faults are mainly normal faults. The measured dip angles of faults revealed moderate to steep dip angles that range from 65° to 80°. Most of the investigated faults are found dissecting the Miocene rock units. Based on the inversion result of DCR soundings, five resistivity sections were designed to delineate the regional geology, structure, and hydrogeological setting. The resistivity sections A-A' and B-B' were built parallel to the fold axis in directions W-E, SW-NE.

On the other hand, the resistivity sections C-C', D-D,' and E-E' are perpendicular to the fold axis NW-SE directions. Moreover, the output geological, structure geometrical parameters and available hydrogeological data are integrated to be considered in constructing the resistivity section (fig. 9). The cross sections show that the normal faults run through the Miocene rocks between soundings. The increase in Miocene rock thickness at the downthrows of the normal fault indicates that these faults were active during Miocene times. Moreover, the horst, graben, and step faults are shown clearly in the cross sections, which have a vital role in determining the hydrogeologic characterization.

The distribution of subsurface structures, faults, folds, and fractures controls the underground water in the study area. Hydrogeologically, based on the borehole data and layer resistivity distribution. The Miocene aquifers

show toward the anticline fold limps directions, which represent a medium to low resistivity layer; the Oligocene sand and gravel aquifers show around the anticline fold core, which was represented by sand, gravel, and basalt fragments. High resistivity values represent the Oligocene aquifers compared to the Miocene aquifers. (Fig.9)

REFERENCES

1. Anomohanran O, Ofomola MO, Okocha FO (2017) Investigation of groundwater in parts of Ndokwa district in Nigeria using geophysical logging and electrical resistivity methods: implications for groundwater exploration. J Afr Earth Sci 129:108–116. https://doi.org/10.1016/j.jafrearsci.2016.12.008.

2. Crestani E, Camporese M, Belluco E, Bouchedda A, Gloaguen E, Salandin P (2022) Large-Scale Physical Modeling of Salt-Water Intrusion. Water, 14, 1183. https:// doi.org/10.3390/w14081183

3. Abotalib, EssamHeggy, Mohamed EL Bastawesy, Esam Ismail, Ahmed Gad, Mohamed Attwa (2021) Groundwater mounding: A diagnostic feature for mapping aquifer connectivity in hyper-arid deserts, 20 December 2021, Volume 801, 149760

4. Attwa M, El Bastawesy M, Ragab D, Othman A, Assaggaf HM, Abotalib AZ (2021) Toward an integrated and sustainable water resources management in structurally-controlled watersheds in desert environments using geophysical and remote sensing methods. Sustainability. 13(7):4004. https://doi.org/10.3390/su13074004.

5. Abdullateef Lawal, Manu Nasiru, UsmanYahyaYero, Abdulmajid Isa Jibrin, Yusuf Abdulmumin (2022) Remote sensing and electrical resistivity in delineating groundwater potential zones in Precambrian basement complex rocks: a case study from northeastern Nigeria. Arabian Journal of Geosciences **volume 15**, Article number: 803

6. Ravindra K Gupta, Mohit Agrawal, Sanjit Kumar Pal, Rajwardhan Kumar (2019) Saurabh Srivastava Environmental Earth Sciences (2019) volume 78, Article number: 226.

7. Attwa M, Henaish A (2018) Regional structural mapping using a combined geological and geophysical approach - A preliminary study at Cairo-Suez district, Egypt. Journal of African Earth Sciences,144, 104-121. https://doi.org/10.1016/j.jafrearsci.2018.04.010

8. Attwa et al., 2021. Hydrogeological characterization

9. Moustafa, A.R, Yehia, M.A, Abdel Tawab, S (1985) structural setting of the area east of Cairo, Maadi and Helwan-MERC Ain Shams univ, Sci. Res. Ser 5:40-46.

10. Moustafa AR, Abd-Allah MA (1991) Structural setting of the central part of the Cairo-Suez District. Middle East Research Center, Ain Shams University, Earth Science Series 5, 133-145.

11. Attwa M, Henaish A (2018) Regional structural mapping using a combined geological and geophysical approach - A preliminary study at Cairo-Suez district, Egypt. J Afr Earth Sci 144:104-121. https://doi.org/10.1016/j.jafrearsci.2018.04.010.

12. Henaish, A., Kharbish, S., 2020. Linkage style of rift-associated fault arrays: insights from central Cairo-Suez district, Egypt. Carpathian Journal of Earth and Environmental Sciences, February 2020, Vol. 15, No. 1, p. 189 – 196.

13. Ahmed M Eldosouky, Luan Thanh Pham, Ahmed Henaish, (2022) High precision structural mapping using edge filters of potential field and remote sensing data: A case study from Wadi Umm Ghalqa area, South Eastern Desert, Egypt. The Egyptian Journal of Remote Sensing and Space Science, Volume 25: 501-513.

14. Henaish A (2018a) Soft-linkage transfer zones: Insights from the Northern Eastern Desert, Egypt. Marine and Petroleum Geology, 95, 265.

15. Henaish, A., Kharbish, S., 2020 Linkage style of rift-associated fault arrays: insights from central Cairo-Suez district, Egypt. Carpathian Journal of Earth and Environmental Sciences, February 2020, Vol. 15, No. 1, p. 189 - 196

16. Moustafa AR, El Badrawy R, Gibali H, (1998) Pervasive E-ENE oriented faults in northern Egypt and their effect on the development and inversion of prolific sedimentary basins. In: 14th E.G.P.C. Petrol. Conf. Cairo, 1, 51-67.

17. Henaish A (2018b). Fault-related domes: Insights from sedimentary outcrops at the northern tip of the Gulf of Suez rift, Egypt. Marine and Petroleum Geology, 91, 202-210. https://doi.org/10.1016/j.marpetgeo.2018.01.009

18. Attwa M, Henaish A, Zamzam S (2020) Hydrogeologic characterization of a fault-related dome Using outcrop, borehole and electrical resistivity data. Natural Resources Research, 29(2), 1143-1161.https://doi.org/10.1007/s11053-019-09504-6.

19. El Haddad, I. M. (2002). Hydrogeological studies and their environmental impact on future management and sustainable development of the new communities and their surroundings, east of the Nile Delta, Egypt. Dissertation, University of Mansoura, Egypt.

20. Abou Heleika, M. M., Atwia, M. G. (2015) Integrated electrical resistivity and hydrogeological studies for delineating the Miocene aquifer at Eastern side of Nile Delta, Egypt. Arabian Journal of Geosciences, 8, 4657. https://doi.org/10.1007/s12517-014-1575-8.

21. Gouasmia, M, Khorchani, H, Mhamdi A, et al (2018) Hydrogeological characterization of a carbonate aquifer using geophysical and geochemical approach: case of the Krachoua Formation in Tataouine area, Southern Tunisia. Arab J Geosci 11, 786. https://doi.org/10.1007/s12517-018-4150-x.

22. Ebong ED, Abong, AA, Ulem EB et al. (2021) Geoelectrical resistivity and geological characterization of hydro structures for groundwater resource appraisal in the Obudu Plateau, southeastern Nigeria. Nat Resource Res, 30, 2103–2117. https://doi.org/10.1007/s11053-021-09818-4.

23. Maury S, Balaji S (2013) Geoelectrical method in the investigation of groundwater resource and related issues in Ophiolite and Flysch formations of Port Blair, Andaman Island, India. Environ. Earth Sci. 2013, 71, 183–199.

24. Bobachev A (2008) IPI2Win V 3.1.0 2C: User's Guide, Programs Set for VES Data Interpretation; Department of Geophysics, Moscow State University: Moscow, Russia, 2008.

25. Basokur A.T, Akça I, Siyam N.W.A (2007) Hybrid genetic algorithms in view of the evolution theories with application for the electrical sounding method. Geophysics. Prospect. 2007, 55, 393–406.

26. Akça I, Basokur AT (2010) Extraction of structure-based geoelectric models by hybrid genetic algorithms. Geophysics, 75, 15-22.